

Physics-Based Analytical Model of the Planetary Bow Shock Position and Shape

. Kotova¹, M. Verigin¹, T. Gombosi², K. Kabin³, J. Slavin², and V. Bezrukih¹

¹Space Research Institute of RAS, Moscow, Russia, kotova@iki.rssi.ru

²University of Michigan, Ann Arbor, Michigan, United States, tamas@umich.edu

³Royal Military College of Canada, Kingston, Ontario, Canada, Konstantin.Kabin@rmc.ca

Corresponding author: Galina Kotova (kotova@iki.rssi.ru)

Key Points:

- For an arbitrary direction of the interplanetary magnetic field the bow shock nose is skewed from the direction of the solar wind flow.
- Asymptotic bow shock slope downstream from the planet in MHD approximation is calculated analytically in the skewed reference frame.
- Analytical expressions are obtained for the bow shock parameters as functions of the solar wind parameters.

This is the author manuscript accepted for publication and has undergone full peer review but has not been through the copyediting, typesetting, pagination and proofreading process, which may lead to differences between this version and the [Version of Record](#). Please cite this article as doi: [10.1029/2021JA029104](https://doi.org/10.1029/2021JA029104).

This article is protected by copyright. All rights reserved.

Abstract

In studies of physical processes near planetary bow shocks, empirical models of the latter are usually used. While computational MHD or kinetic models of bow shocks are often more accurate, their computationally extensive nature limits their applicability to routine analysis of large volumes of data. We suggest an analytical model of the bow shock position based on MHD calculations and accurate analytical solutions. The analytical expressions for the bow shock position and shape include the following parameters: the distance of the bow shock nose point from the planet, radii of curvature and bluntnesses of the shock surface at this point and a parameter describing the transition to the asymptotic downstream slope of the shock. It is shown that for an analytical description of the surface of the shock it is sufficient to approximate its radius of curvature and bluntness in two perpendicular planes. Another parameter used in this model is the bow shock skewing angle, appearing when the interplanetary magnetic field is directed at an angle with respect to the solar wind velocity. This parameter naturally vanishes when the magnetic field of the solar wind is directed either parallel or perpendicular to the velocity vector. The exact analytical solution for the asymptotic downstream slope of the MHD Mach cone is modified to take into account the skewing angle of the bow shock.

Plain Language Summary

The solar wind is a stream of charged particles emitted by the Sun. The interplanetary magnetic field embedded in the solar wind is the solar magnetic field dragged out from the solar corona. Bulk velocity of the solar wind is higher than sonic velocity and higher than the velocity of Alfvén waves. Planets with their magnetospheres and ionospheres create obstacles to the solar wind flow, and in front of planetary magnetosphere, bow shock forms, similar to the shock wave formation ahead of a supersonic aircraft. To study many physical processes in the vicinity of planets it is necessary to have a useful physical model of the position and shape of the bow shock. MHD and kinetic simulations provide accurate models but they are too computationally extensive. To analyze experimental data empirical models are mainly used, but they are not equally accurate in all space. We suggest an analytical model of the bow shock position and shape based on MHD calculations and accurate analytical solutions. This model is easy to use and describes the bow shock well near the planet and far downstream.

1 Introduction

Studies of physical processes near the Earth and near other planets often require a robust and convenient bow shock model for data classification and analysis. These processes include: electron and ion foreshock formation, plasma wave generation by secularly and diffusely reflected ions, mechanisms of the solar wind deceleration in the shock foot and shock itself, plasma wave propagation along the shock surface, processes of shock overshoot formation, plasma turbulence generation inside the magnetosheath, generation of micropulsations at the bow shock and magnetopause, etc.

The bow shock can be modeled using several different approaches. For example, magneto-hydrodynamics (MHD) description of solar wind interaction with a planet is often used (e.g., Stahara, 2002; Cairns and Lyon, 1995, Gombosi, 1999; Kabin et al., 2000; Chapman et al., 2004; Ledvina et al., 2008, Mejnertsen et al., 2018). This approach usually allows achieving good agreement with experimental data (Winterhalter et al., 1984; Merka et al., 2003). Some bow shock models are based on kinetic simulations or on combinations of MHD with kinetics

(Brecht, 1997; Ledvina et al., 2008; Pokhotelov et al., 2013). All these computational models require significant processor time. They provide a reliable basis for studying the bow shock but cannot be used in practice to analyze a large amount of data obtained under various solar wind conditions.

Another common approach to describing the bow shock shape and position utilizes empirical models fitted to observations. During the last 20-30 years a large amount of experimental data was obtained in the vicinity of planetary bow shocks (Phobos, Interball / Magion-4, Wind, Geotail, Mars Express Mission, Cluster, THEMIS, etc). These observations are accompanied by almost continuous monitoring of the undisturbed solar wind (IMP-8, Wind, ACE). These data served as the basis for various empirical models of the bow shock (Fairfield, 1971, 2001; Formisano, 1979; Slavin and Holzer, 1981; Němeček and Šafránková, 1991; Peredo et al., 1995; Chao et al., 2002; Merka et al., 2003; Chapman and Cairns, 2003; Dmitriev et al., 2003, Jelínek et al., 2012; Meziane et al., 2014, Hall et al, 2019, Lu et al., 2019, Wang et al., 2020). Such models are very convenient and easy to use; they also agree well with the average location and shape of bow shock. However, their applicability is always limited by the range of the solar wind parameters used in their construction. Such models often have to be scaled in order to agree with the observations for any particular event. The existing models do not take into account the bow shock slope at infinity. Besides, they do not consider the influence of polytropic index on the shape of the bow shock.

To address the shortcomings of both computational and empirical models M.I. Verigin with co-authors developed a semiempirical approach for modeling different plasma boundaries and regions in space (Verigin et al., 1997a, b, 1999, 2001a,b, 2003a,b; 2004a,b, 2009, 2018; Verigin, 2004; Kotova et al., 2005, 2015, 2020a,b). This approach is based on maximum use of exact analytical solutions that describe some characteristic properties of the phenomenon, e.g., the asymptotic MHD Mach cone. The parameters used in these semi-empirical modes have clear physical meaning.

At large Alfvén Mach numbers, Gas Dynamics (GD) provides an accurate approximation of the planetary bow shocks. A detailed GD analytical model of a bow shock for obstacles of various shapes (ranging from a hyperboloid to a stub cylinder) was developed by Verigin et al. (2003a). More recently, Kotova et al (2020a) used a similar approach to calculate the parameters of planetary bow shocks for interplanetary magnetic field either parallel or perpendicular to the solar wind flow. Below we present an extension of these two models for an arbitrary direction of the magnetic field. The resulting model is applicable for any direction of the interplanetary magnetic field, any polytropic index γ , any Alfvén M_A , and sonic M_S Mach numbers ($M_A^2 = \frac{4\pi\rho V^2}{B^2}$, $M_S^2 = \frac{\rho V^2}{\gamma p}$, ρ – plasma mass density, V – plasma bulk velocity, B – magnetic field magnitude, p – plasma thermal pressure), and various shapes of the obstacle. We also ensure that our new model agrees with the analytic description of the bow shock slope at infinity obtained by Verigin et al (2003b). Thus, we propose a model for the entire surface of the bow shock, which can be used in a wide range of solar wind parameters for various obstacles.

2 General definitions

It is convenient to describe the bow shock using Geocentric InterPlanetary Medium (GIPM) coordinates. This reference frame was introduced by Bieber & Stone (1979) to study the

leakage of energetic electrons from the magnetosphere; it was also used for bow shock studies (Peredo et al., 1995; Verigin et al., 2001a, b; Dmitriev et al., 2003; and others). In GIMP coordinates, the velocity and magnetic field vectors of the undisturbed flow lie in the (X, Y) plane. The X axis is antiparallel to the undisturbed solar wind velocity vector, the Y axis is directed so that the magnetic field vector lies in the second - fourth quadrant of the (X, Y) plane, and the Z axis completes the right-hand system. The interplanetary field azimuth in GIMP coordinates lies either between 90° and 180° or between 270° and 360° .

We assume that the obstacle is rotationally symmetric with respect to the X – axis, see figure 1. In addition to the radius of curvature, R_o , we use bluntness parameter, b_o , to characterize the shape of the boundary as defined below. Near the nose point, the shape of the obstacle can be approximated using a series expansion as:

$$x(\rho) = r_o - \rho^2/2R_o + b_o(\rho^4/8R_o^3) - \dots,$$

where $\rho = \sqrt{y^2 + z^2}$. Here R_o is the radius of curvature of the obstacle at the nose point, and b_o is the dimensionless bluntness coefficient. For a paraboloid $b_o = 0$, for an ellipsoid $b_o < 0$ at the nose, for a sphere $b_o = -1$, and for hyperboloids $b_o > 0$.

If the magnetic field is either parallel or perpendicular to the solar wind velocity, the nose point of the bow shock is located on the X axis of the GIMP coordinates. In these cases the bow shock is either axially symmetric or symmetric with respect to the (X, Y) and (X, Z) planes, respectively. Similarly to the obstacle, we describe the subsolar shape of the bow shock using the radius of curvature, R_s , of the shock and its bluntness, b_s .

Following Verigin et al., (2003a) and Kotova et al. (2020a, b) we define the planetary bow shock shape by the expression:

$$\rho^2(x) = 2R_s(r_s - x) + \tan^2 \omega_{as} \cdot (r_s - x)^2 \cdot \left(1 + \frac{b_s \tan^2 \omega_{as} - 1}{1 + d_s \frac{r_s - x}{R_s}} \right), \quad \rho = \sqrt{y^2 + z^2}. \quad (1)$$

The additional parameter d_s characterizes the transition from the predominance of the parameters of the bow shock subsolar region to the region where the asymptotic slope dominates. Angle ω_{as} is the asymptotic slope of the bow shock far downstream (Slavin et al., 1984) calculated following Verigin et al., 2003b. For general orientation of the interplanetary magnetic field the parameters of expression (1) r_s , R_s , b_s d_s , as well as the values of ω_{as} depend on the clock angle $\varphi = \cos^{-1}(y/\rho)$.

3 Skewing angle

In general case of an axially symmetric obstacle for an arbitrary direction of the interplanetary magnetic field, the only symmetry plane of the bow shock surface is the (X, Y) plane of the GIMP frame containing the solar wind velocity and magnetic field vectors.

We define the nose of the bow shock as the point behind which the plasma flows along the normal to the shock front. To quantify the displacement of the nose point from the X -axis we introduce skewing angle α_{vn} which is defined as the angle between the upstream velocity direction and the direction of the shock normal at the nose point of the bow shock (Fig. 2). This skewing angle is an additional parameter used in our bow shock model. The angle between the upstream magnetic field direction and the direction of the shock normal at the nose point of the bow shock $\vartheta_{bn} = \vartheta_{bv} - \alpha_{vn}$. We furthermore define a new coordinate system frame (X_s, Y_s, Z_s)

which is obtained by rotating the X and Y axis of the GIPM system around Z axis by the angle α_{vn} . This reference frame is used in section 4 and later for approximating the bow shock surface calculated in MHD by expression (1).

The skewing angle can be calculated using MHD Rankine-Hugoniot conditions as follows. At the nose point, by definition, the tangential component of the velocity behind the shock is equal to zero:

$$V_{t1} = V_t + B_t \frac{V_n}{B_n} \frac{(1-\varepsilon)}{\left(\frac{\varepsilon^4 \rho V_n^2}{B_n^2} - 1\right)} = 0, \quad (2)$$

where the subscripts t and n refer to the tangential and normal components, respectively, of vectors \mathbf{V} and \mathbf{B} . In our paper, the upstream parameters are used without subscripts and downstream values marked by subscript "1". Here ρ is the mass density, ε is an inverse compression ratio $\varepsilon = \varepsilon(\gamma, M_S, M_A, \vartheta_{bn}, \alpha_{vn}) = \rho/\rho_1 = V_{n1}/V_n$ which can be calculated from the following cubic equation (e.g., Petrinec and Russell (1995); Kabin, 2001):

$$a\varepsilon^3 + b\varepsilon^2 + c\varepsilon + d = 0, \text{ where} \quad (3)$$

$$a = (\gamma + 1) M_A^6 \cos^6 \alpha_{vn},$$

$$b = -(\gamma - 1) M_A^6 \cos^6 \alpha_{vn} - (\gamma + 2) M_A^4 \cos^4 \alpha_{vn} \cos^2(\vartheta_{bv} - \alpha_{vn}) - \left(\gamma + 2 \left(\frac{M_A}{M_S}\right)^2\right) M_A^4 \cos^4 \alpha_{vn}, \quad (4)$$

$$c = (\gamma - 2 + \gamma \cos^2(\vartheta_{bv} - \alpha_{vn})) M_A^4 \cos^4 \alpha_{vn} + \left(\gamma + 1 + 4 \left(\frac{M_A}{M_S}\right)^2\right) M_A^2 \cos^2 \alpha_{vn} \cos^2(\vartheta_{bv} - \alpha_{vn}),$$

$$d = -\cos^2(\vartheta_{bv} - \alpha_{vn}) \left((\gamma - 1) M_A^2 \cos^2 \alpha_{vn} + 2 \left(\frac{M_A}{M_S}\right)^2 \cos^2(\vartheta_{bv} - \alpha_{vn}) \right)$$

Relation (2) can be transformed to:

$$\tan \alpha_{vn} = \tan(\vartheta_{bv} - \alpha_{vn}) \frac{(1-\varepsilon)}{\varepsilon M_A^2 \frac{\cos^2 \alpha_{vn}}{\cos^2(\vartheta_{bv} - \alpha_{vn})} - 1}, \quad (5)$$

Equations (3) and (5) are solved to calculate α_{vn} .

Figure 3 presents examples of α_{vn} calculations as a function of ϑ_{bv} for $\gamma = 5/3$ and different M_S and M_A . When the sonic Mach number is quite high and the Alfvén Mach number is low, Figure 3 shows that the bow shock nose point can deviate by up to 30 degrees from the solar wind velocity direction.

4 Asymptotic bow shock Mach cone in a skewed reference frame

Verigin et al. (2003) derived an implicit equation, which enables the calculation of the asymptotic downstream slope of MHD Mach cone for any clock angle for arbitrary M_S , M_A , and ϑ_{bv} angle. Since their calculation was done in the GIPM reference frame, it is necessary to reformulate the procedure for the skewed coordinate system (Fig. 2). For this derivation it is

convenient to use a cylindrical (X_S, ρ_S, φ_S) coordinates with the clock angle φ_S measured from the + Y_S direction. In this reference frame:

$$\mathbf{B} = B(-\cos(\vartheta_{bv} - \alpha_{vn}), \sin(\vartheta_{bv} - \alpha_{vn}) \cos \varphi_S, -\sin(\vartheta_{bv} - \alpha_{vn}) \sin \varphi_S) \quad (6)$$

$$\mathbf{V} = V(-\cos \alpha_{vn}, -\sin \alpha_{vn} \cos \varphi_S, \sin \alpha_{vn} \sin \varphi_S).$$

Here it can be assumed that $0 \leq \vartheta_{bv} \leq \pi/2$ since the velocity of the MHD waves is independent of the polarity of the magnetic field.

Sufficiently far downstream (here and further far downstream means far behind the planet), the general bow shock surface defined as $F(X_S, \rho_S, \varphi_S)=0$ simplifies to:

$$F(X_S, \rho_S, \varphi_S) \rightarrow X_S + q(\varphi_S) \rho_S = 0 \text{ as } X_S \rightarrow -\infty. \quad (7)$$

The asymptotic slope of the shock is then defined for all clock angles as

$$\tan \omega(\varphi_S) \Big|_{\varphi_S = \text{const}} = -\frac{d\rho_S}{dX_S} = \frac{1}{q(\varphi_S)} \quad (8)$$

Thus, computing the asymptotic MHD Mach cone reduces to determining function $q(\varphi_S)$.

Following Verigin et al. (2003) we proceed as follows. Using equation (7) we can calculate the shock normal \mathbf{n} in the far downstream area as:

$$\mathbf{n} = \frac{\nabla F}{|\nabla F|} = \frac{(1, q, q')}{\sqrt{1+q^2+q'^2}}, \quad q = q(\varphi_S), \quad q' = dq/d\varphi_S \quad (9)$$

Taking into account relations (6), $\cos \alpha_{vn}$ and $\cos \vartheta_{bn}$ can be determined as:

$$\cos \alpha_{vn} = \mathbf{V} \cdot \mathbf{n} / V = \frac{-\cos \alpha_{vn} - q \sin \alpha_{vn} \cos \varphi_S + q' \sin \alpha_{vn} \sin \varphi_S}{\sqrt{1+q^2+q'^2}} \quad (10)$$

$$\cos \vartheta_{bn} = \mathbf{B} \cdot \mathbf{n} / B = \frac{-\cos(\vartheta_{bv} - \alpha_{vn}) + q \sin(\vartheta_{bv} - \alpha_{vn}) \cos \varphi_S - q' \sin(\vartheta_{bv} - \alpha_{vn}) \sin \varphi_S}{\sqrt{1+q^2+q'^2}}$$

Far downstream of the obstacle MHD Rankine-Hugoniot conditions (Landau & Lifshitz, 1984) permit to obtain the following relation for fast and slow MHD shocks (Verigin et al., 2003b, Kabin, 2001):

$$(M_A^2 + M_S^2) \cos^2 \alpha_{vn} - M_A^2 M_S^2 \cos^4 \alpha_{vn} - \cos^2 \vartheta_{bn} = 0 \quad (11)$$

Relation (11) together with (10) leads to the nonlinear transcendental differential equation for the function $q(\varphi_S)$:

$$\begin{aligned} & (M_A^2 + M_S^2)(-\cos \alpha_{vn} - q \sin \alpha_{vn} \cos \varphi_S + q' \sin \alpha_{vn} \sin \varphi_S)^2 = \\ & (-\cos(\vartheta_{bv} - \alpha_{vn}) + q \sin(\vartheta_{bv} - \alpha_{vn}) \cos \varphi_S - q' \sin(\vartheta_{bv} - \alpha_{vn}) \sin \varphi_S)^2 + \\ & \frac{M_A^2 M_S^2 (-\cos \alpha_{vn} - q \sin \alpha_{vn} \cos \varphi_S + q' \sin \alpha_{vn} \sin \varphi_S)^4}{1+q^2+q'^2} \end{aligned} \quad (12)$$

To find a solution of equation (12) it is helpful to introduce two new functions

$$\begin{aligned} p &= q' \sin \varphi_S - q \cos \varphi_S \\ t &= q' \cos \varphi_S + q \sin \varphi_S \end{aligned} \quad (13)$$

Then (12) is transformed to:

$$(M_A^2 + M_S^2)(-\cos \alpha_{vn} + p(\varphi_S) \sin \alpha_{vn})^2 = (\cos(\vartheta_{bv} - \alpha_{vn}) + p(\varphi_S) \sin(\vartheta_{bv} - \alpha_{vn}))^2 + \frac{M_A^2 M_S^2 (-\cos \alpha_{vn} + p(\varphi_S) \sin \alpha_{vn})^4}{1 + p(\varphi_S)^2 + t(\varphi_S)^2}, \quad (14)$$

which can be solved for $t(\varphi_S)$:

$$t(\varphi_S)^2 = \frac{M_A^2 M_S^2 (-\cos \alpha_{vn} + p(\varphi_S) \sin \alpha_{vn})^4}{D(p(\varphi_S))} - p(\varphi_S)^2 - 1, \quad (15)$$

where

$$D(p(\varphi_S)) = (M_A^2 + M_S^2)(-\cos \alpha_{vn} + p(\varphi_S) \sin \alpha_{vn})^2 - (\cos(\vartheta_{bv} - \alpha_{vn}) + p(\varphi_S) \sin(\vartheta_{bv} - \alpha_{vn}))^2$$

Differentiating (15) we get

$$\begin{aligned} \frac{dt(\varphi_S)^2}{dp(\varphi_S)} &= -2p(\varphi_S) + 4 \frac{M_A^2 M_S^2}{D(p(\varphi_S))} (-\cos \alpha_{vn} + p(\varphi_S) \sin \alpha_{vn})^3 \sin \alpha_{vn} - \\ &2 \frac{M_A^2 M_S^2}{D(p(\varphi_S))^2} (-\cos \alpha_{vn} + p(\varphi_S) \sin \alpha_{vn})^4 ((M_A^2 + M_S^2)(-\cos \alpha_{vn} + \\ &p(\varphi_S) \sin \alpha_{vn}) \sin \alpha_{vn} - (\cos(\vartheta_{bv} - \alpha_{vn}) + p(\varphi_S) \sin(\vartheta_{bv} - \alpha_{vn})) \sin(\vartheta_{bv} - \alpha_{vn})) \end{aligned} \quad (16)$$

Which equals

$$\frac{dt(\varphi_S)^2}{dp(\varphi_S)} = 2 \frac{t(\varphi_S)}{\tan \varphi_S} \quad (17)$$

using (13). Thus, we obtain an equation for $p(\varphi_S)$:

$$\begin{aligned} \frac{1}{\tan \varphi_S} \sqrt{\frac{M_A^2 M_S^2}{D(p(\varphi_S))^2} (-\cos \alpha_{vn} + p(\varphi_S) \sin \alpha_{vn})^4 - p(\varphi_S)^2 - 1} &= -p(\varphi_S) + \\ \frac{2M_A^2 M_S^2}{D(p(\varphi_S))} (-\cos \alpha_{vn} + p(\varphi_S) \sin \alpha_{vn})^3 \sin \alpha_{vn} - \frac{M_A^2 M_S^2}{D(p(\varphi_S))^2} (-\cos \alpha_{vn} + \\ p(\varphi_S) \sin \alpha_{vn})^4 ((M_A^2 + M_S^2)(-\cos \alpha_{vn} + p(\varphi_S) \sin \alpha_{vn}) \sin \alpha_{vn} - (\cos(\vartheta_{bv} - \alpha_{vn}) + \\ p(\varphi_S) \sin(\vartheta_{bv} - \alpha_{vn})) \sin(\vartheta_{bv} - \alpha_{vn})) \end{aligned} \quad (18)$$

However the equation (17) can be easily solved for the inverse function $\varphi_S(p)$

$$\varphi_S(p) = \begin{cases} \tan^{-1} \frac{\sqrt{t^2(p)}}{\frac{1}{2} \frac{dt^2(p)}{dp}}, & \frac{dt^2(p)}{dp} > 0 \\ \pi - \tan^{-1} \frac{\sqrt{t^2(p)}}{\frac{1}{2} \frac{dt^2(p)}{dp}}, & \frac{dt^2(p)}{dp} < 0 \end{cases} \quad (19)$$

Figure 4 presents $t^2(p)$ function (16) for $M_S = 6$, $M_A = 3$, $\vartheta_{bv} = 70^\circ$, $\alpha_{vn} = 4.3^\circ$. Note, that only sections where $t^2 > 0$, shown with solid lines in Figure 4, are physically meaningful. Function $t^2(p)$ has vertical asymptotes at

$$p_{as1} = \frac{\sqrt{M_A^2 + M_S^2 \cos \alpha_{vn} + \cos(\vartheta_{bv} - \alpha_{vn})}}{\sqrt{M_A^2 + M_S^2 \sin \alpha_{vn} - \sin(\vartheta_{bv} - \alpha_{vn})}}, \quad (20)$$

$$p_{as2} = \frac{\sqrt{M_A^2 + M_S^2 \cos \alpha_{vn} - \cos(\vartheta_{bv} - \alpha_{vn})}}{\sqrt{M_A^2 + M_S^2 \sin \alpha_{vn} + \sin(\vartheta_{bv} - \alpha_{vn})}}.$$

There are generally four roots p_{1-4} of $t^2(p)=0$ equation. $\varphi_S(p)$ dependencies calculated with relations (19) for values of p between the negative asymptote (20) and p_1 , and between p_4 and the positive asymptote correspond to slow shocks. $\varphi_S(p)$ dependencies calculated for values of p between p_2 and p_3 correspond to fast shocks.

Now we can calculate function $p(\varphi_S)$ for $0 \leq \varphi_S \leq \pi$ and, hence, $t(\varphi_S)$, $q(\varphi_S)$, $\rho(\varphi_S)$, and $\omega(\varphi_S)$ from relations (13, 8), respectively.

5 Fitting of MHD calculations

Our model of the bow shock is constructed on the basis of 26 fine resolution 3D MHD simulations, performed at the University of Michigan. These MHD simulations used adaptive grids with nearly $3 \cdot 10^6$ cells (Fig.5). All linear dimensions are given in terms of r_o . The MHD simulations used 2 types of obstacles – paraboloid of revolution and hemisphere with elongated cylindrical tail, 2 values of polytropic index γ , 5/3 and 2.0, and for different conditions in the solar wind: different M_S , M_A and magnetic field direction ϑ_{bv} .

The determination of the parameters of the model - r_s , R_s , b_s , d_s , α_{vn} - is based on the approximation of MHD calculations of the bow shock shape and position for different obstacles by expression (1). Expression (1) can be used directly for fitting the calculated bow shock surface only if the interplanetary magnetic field is parallel to the solar wind velocity. In all other cases of an arbitrary magnetic field direction the parameters of expression (1) depend on the clock angle $\varphi = \cos^{-1}(y/\rho)$. In the case of magnetic field perpendicular to the flow velocity, Kotova et al., 2020a used the following expressions to describe the dependence of parameters R_s , b_s , and d_s on the clock angle:

$$R_s = \frac{R_{sy}R_{sz}}{R_{sy} \sin^2 \varphi + R_{sz} \cos^2 \varphi}, \quad b_s = b_{sz} \sin^2 \varphi + b_{sy} \cos^2 \varphi, \quad d_s \sim const., \quad (21)$$

where R_{sy} and R_{sz} are curvature radii in the plane (X, Y) containing magnetic field and velocity vectors and in the perpendicular plane (X, Z) , respectively. The bluntnesses b_{sy} and b_{sz} were defined similarly.

In order to account for arbitrary angle of the interplanetary magnetic field direction with respect to the solar wind velocity we checked the usage of relations (21) in the skewed coordinate system. For such checking, we fitted the bow shock profiles individually in every $\varphi_s = const$ plane and thus obtain numerical functions $r_s(\varphi_s)$, $R_s(\varphi_s)$, $b_s(\varphi_s)$ and $d_s(\varphi_s)$. Figure 6 illustrates the accuracy of relations (21) for approximating these numerical functions. As expected the position of the nose point is independent of φ_s , while $R_s(\varphi_s)$ and $b_s(\varphi_s)$ are satisfactorily approximated by expressions (21). The parameter d_s did not show any clear dependence on φ_s , and it was assumed to be constant similarly to the case of magnetic field perpendicular to the solar wind velocity. Relations (21) make it possible to use the expression (1) to approximate the MHD simulations of the entire bow shock surface and to determine the parameters of the model: r_s , R_{sy} , R_{sz} , b_{sy} , b_{sz} , d_s , α_{vn} . And in the following approximations we do not use equation (5) for the skewing angle, but instead find it as an additional fitting parameter of the model.

Table 1 presents the parameters of the model obtained when fitting all the 26 cases of MHD bow shock simulations by expression (1). In all the simulations the obstacle parameters are: $r_o=1$ and $R_o=1$. The last column presents the values of residuals $\sigma = \Sigma D_i^2/N$ (in units of r_o^2) for our fitting procedure. Here D_i stands for the distance of the i -th point (X_{Si}, Y_{Si}, Z_{Si}) on the simulated bow shock surface from the surface described by (1) and (21) with 7 fitting parameters $r_s, R_{sy}, R_{sz}, b_{sy}, b_{sz}, d_s, \alpha_{vn}$. N is the number of points in the related MHD simulation. N values vary from to 3700 to 8000 points. The values of the residuals are consistently small, indicating good fit obtained with equation (1) for a wide range of obstacles and upstream conditions.

Figure 7 gives two examples of such fitting for solar wind parameters $\gamma=5/3, M_S = 6, M_A = 5, \vartheta_{bv} = 30^\circ$ (Fig.7a,b) and $\gamma=5/3, M_S = 6, M_A = 3, \vartheta_{bv} = 70^\circ$ (Fig.7c,d). Since the bow shock is symmetric relative to the (X,Y) plane, in the plane (X, Z) the bow shock fitting is shown only for $Z < 0$. The calculated shock parameters are listed in Table 1, lines 3 and 9, respectively.

Figure 7 show that the relatively simple expression (1) provides very good description of the bow shock shape. The accuracy of this approximation appears to be lowest near the negative part of the Y axis of the GIPM coordinates. This region is further discussed at the end of the next section.

6 Transformation of GD bow shock parameters into the MHD regime

To calculate the parameters of Eq.1 as functions of the upstream conditions for the MHD bow shock, we proceed from the formulas obtained for the gas-dynamic bow shock (Appendix, relations 35-43 in Verigin et al., 2003a). Parameters $r_s, R_{sy}, R_{sz}, b_{sy}, b_{sz}$ refer to the nose point of the bow shock, and, therefore, can be obtained by comparing the expansion rate of central flow tube after shock crossing in MHD and GD cases.

In the case of gas-dynamic flow, the relative expansion rate of the cross-section S of the central flow tube behind the shock wave (e.g., Biermann et al., 1967; Wallis, 1973):

$$\frac{1}{S} \frac{dS}{dx} = -\frac{1}{\rho V} \frac{d(\rho V)}{dx} = -\frac{2}{R_s} \cdot \frac{1-\varepsilon}{\varepsilon}. \quad (22)$$

For the MHD flow this expression can be rewritten as (Kotova et al., 2020b):

$$\frac{1}{S} \frac{dS}{dx} = -\frac{R_{sy}+R_{sz}}{R_{sy}R_{sz}} \frac{1-\varepsilon}{\varepsilon} \frac{1}{\Gamma}, \quad \text{where } \Gamma = \Gamma(\varepsilon, \gamma, M_A, M_S, \vartheta_{bv}, \alpha_{vn}). \quad (23)$$

$$\begin{aligned} & \frac{1}{\Gamma} \\ &= \frac{\varepsilon M_A^2 \cos^2 \alpha_{vn}}{\varepsilon M_A^2 \cos^2 \alpha_{vn} - \cos^2(\vartheta_{bv} - \alpha_{vn})} \\ &= \frac{\sin(\vartheta_{bv} - \alpha_{vn})(\sin(\vartheta_{bv} - \alpha_{vn}) + \tan \alpha_{vn} \cos(\vartheta_{bv} - \alpha_{vn}))(\varepsilon M_A^2 \cos^2 \alpha_{vn} + \cos^2(\vartheta_{bv} - \alpha_{vn}))}{(\varepsilon M_A^2 \cos^2 \alpha_{vn} - \cos^2(\vartheta_{bv} - \alpha_{vn}))^2} \\ &= \frac{1}{1-\varepsilon} \frac{\cos(\vartheta_{bv} - \alpha_{vn}) \sin(\vartheta_{bv} - \alpha_{vn})(M_A^2 \cos^2 \alpha_{vn} - \cos^2(\vartheta_{bv} - \alpha_{vn}))}{(\varepsilon M_A^2 \cos^2 \alpha_{vn} - \cos^2(\vartheta_{bv} - \alpha_{vn}))^2} \cdot \zeta \end{aligned} \quad (24)$$

where $\zeta = \frac{a_1 \varepsilon^3 + b_1 \varepsilon^2 + c_1 \varepsilon + d_1}{3a \varepsilon^2 + 2b \varepsilon + c}$ with parameters a, b, c defined by (4) and:

$$\begin{aligned}
a_1 &= -6(\gamma + 1) M_A^6 \cos^5 \alpha_{vn} \sin \alpha_{vn} \\
b_1 &= 2M_A^4 \cos^3 \alpha_{vn} \left(\left(3(\gamma - 1)M_A^2 \cos^2 \alpha_{vn} + 2(\gamma + 2) \cos^2(\vartheta_{bv} - \alpha_{vn}) + 2\gamma + \right. \right. \\
&\quad \left. \left. 4 \left(\frac{M_A}{M_S} \right)^2 \right) \sin \alpha_{vn} - (\gamma + 2) \cos \alpha_{vn} \cos(\vartheta_{bv} - \alpha_{vn}) \sin(\vartheta_{bv} - \alpha_{vn}) \right), \\
c_1 &= -2M_A^2 \cos \alpha_{vn} \left(\left(2(\gamma - 2)M_A^2 \cos^2 \alpha_{vn} + \right. \right. \\
&\quad \left. \left. 2\gamma M_A^2 \cos^2 \alpha_{vn} \cos^2(\vartheta_{bv} - \alpha_{vn}) + \left(1 + \gamma + 4 \left(\frac{M_A}{M_S} \right)^2 \right) \cos^2(\vartheta_{bv} - \alpha_{vn}) \right) \sin \alpha_{vn} - \right. \\
&\quad \left. \left(\gamma M_A^2 \cos^2 \alpha_{vn} + 1 + \gamma + 4 \left(\frac{M_A}{M_S} \right)^2 \right) \cos \alpha_{vn} \cos(\vartheta_{bv} - \alpha_{vn}) \sin(\vartheta_{bv} - \alpha_{vn}) \right), \\
d_1 &= 2 \cos(\vartheta_{bv} - \alpha_{vn}) \left((\gamma - 1)M_A^2 \cos \alpha_{vn} \cos(\vartheta_{bv} - \alpha_{vn}) \sin \alpha_{vn} - \left((\gamma - \right. \right. \\
&\quad \left. \left. 1)M_A^2 \cos^2 \alpha_{vn} + 4 \left(\frac{M_A}{M_S} \right)^2 \cos^2(\vartheta_{bv} - \alpha_{vn}) \right) \sin(\vartheta_{bv} - \alpha_{vn}) \right).
\end{aligned} \tag{25}$$

For converting the GD parameters to the MHD ones, the following procedure can be used: (i) the gasdynamic inverse compression ratio is replaced by the root ε of equation (3), corresponding to a fast shock; (ii) the parameter $\varepsilon^* = \varepsilon/(\varepsilon - 1)$ is replaced by $\varepsilon^* \Gamma$; and (iii) M_S is replaced by $M_{asy} = (1 + 1/\text{tg}^2 \omega_{asy})^{1/2}$, calculated for the bow shock asymptotic slope in the Y_S - direction ($\varphi_S = 0^\circ$) and $M_{asz} = (1 + 1/\text{tg}^2 \omega_{asz})^{1/2}$, calculated for the bow shock asymptotic slope in the Z_S - direction ($\varphi_S = 90^\circ$). Thus, the parameters of the model deduced earlier for gas-dynamic flow (see Appendix) are replaced: the subsolar position $r_{sGD}(\varepsilon^*, \gamma, R_o, b_o)$ by $r_{sGD}(\Gamma \varepsilon^*, \gamma, R_o, b_o)$, the radius of curvature $R_{sGD}(\varepsilon^*, \gamma, R_o, b_o)$ by $R_{sGD}(\Gamma \varepsilon^*, \gamma, R_o, b_o)$ and the bluntness $b_{sGD}(M_S)$ by $b_{sGD}(M_{asz})$ or $b_{sGD}(M_{asy})$. Everywhere here ε is calculated from equation (3) for the MHD flow. The parameter d_{sGD} is a function of b_o only and does not change. These converted parameters are normalized to approximate the obtained fitting parameters of the model $r_s, R_{sy}, R_{sz}, b_{sy}, b_{sz}, d_s$.

$$r_{s_norm} - r_o = \Gamma^{-2/3} \cdot (r_{sGD}(\Gamma \varepsilon^*, \gamma, R_o, b_o) - r_o) \cdot (1 + 0.37 \sin \vartheta_{bv}), \tag{26}$$

$$R_{sy_norm} = \Gamma^{-2/3} \cdot R_{sGD}(\Gamma \varepsilon^*, \gamma, R_o, b_o) \cdot (M_{asy}/M_{asz})^{1/2}, \tag{27}$$

$$R_{sz} = R_{sy} \Gamma^{\sin \vartheta_{bv}/2} \tag{28}$$

$$b_{sz_norm} = b_{sGD}(M_{asz}) \cdot \left(\frac{M_{asy}}{M_{asz}} \right)^{-2} + 0.27, \quad b_{sy} = b_{sz} - 0.72 \left(\left(\frac{M_{asy}}{M_{asz}} \right)^2 - 1 \right) \tag{29}$$

$$d_{s_norm} = 0.6 d_{sGD}(b_o) \cdot \left(\frac{M_{asy}}{M_{asz}} \right)^2 \tag{30}$$

Figs. 8 and 9 demonstrate good correspondence of the parameters fitting the MHD bow shock simulations and the normalized parameters. Parameters r_s and R_{sy} are well fitted by

parameters r_{s_norm} and R_{sy_norm} calculated by expressions (26, 27) (Fig.8a, b). Figure 8c demonstrates that the parameter R_{sz} is related to R_{sy} via relation (28).

Expressions (26-28) reduce exactly to those obtained for special cases of interplanetary magnetic field parallel or perpendicular to plasma flow direction by Kotova et al, 2020a.

The expressions for the parameters b_{sy} and b_{sz} (29) are slightly modified as compared to those used by Kotova et al. (2020a). Expressions (29) are checked in Fig.9a,b. For the transition parameter d_s the expression (30) is suggested (Fig.9c). The agreement between d_s and d_{s_norm} however, is noticeably worse than for the other parameters.

Finally, in order to verify the use of equation (5) as a proxy for the skewing angle, the fitting angles α_{vn} (Table 1) are plotted as asterisks in Fig.3. The agreement appears to be good although not excellent.

Figure 10 is similar to Fig.7 and shows the comparison of the bow shock location calculated with expression (1) using relations (5, 26-30) with the bow shock locations extracted from the MHD simulations. The upstream condition of the MHD simulations were $\gamma=5/3$, $M_S=6$, $M_A=5$, $\vartheta_{bv}=45^\circ$ for Fig.10a,b and $\gamma=5/3$, $M_S=6$, $M_A=3$, $\vartheta_{bv}=20^\circ$ for Fig.10c,d (Table 1, lines 14 and 1, respectively). The parameters of the bow shock model were $\alpha_{vn}=3.0$, $r_s=1.31$, $R_{sy}=1.74$, $R_{sz}=1.75$, $b_{sy}=-0.46$, $b_{sz}=-0.01$, $d_s=1.3$ for the first simulation and $\alpha_{vn}=6.0$, $r_s=1.22$, $R_{sy}=1.9$, $R_{sz}=1.8$, $b_{sy}=-0.35$, $b_{sz}=0.15$, $d_s=1.4$, for the second.

Similarly to Fig.7, noticeable discrepancies between the MHD shock and model calculations are sometimes observed in a small region close to the plane (X, Y) of the GIPM system in the negative Y area where the blue curves (approximation) do not coincide with points (MHD calculations). The comparison in the (Z, Y) plane shows that these discrepancies appear only in a very limited area. This may be due to the fact that in MHD calculations the position of the shock wave is determined automatically, and it is in this region that this can lead to errors. Kabin (2001) considered this area in detail and it was demonstrated that fast shock wave does not always exist there (see Fig.10 in Kabin, 2001) and it is not always easy to find the correct bow shock position. It is also possible that the presented analytic model is not flexible enough to describe this area. Anyhow Fig.10b,d shows that these discrepancies are observed in a very limited area, and the model describes the bow shock well both close to the planet and far downstream.

7 Summary

A new analytical model of the bow shock shape formed in the solar wind flow upstream of planets is developed. Our model is shown to be accurate by comparison with high-resolution MHD simulations. The model does not require any significant computational resources and can generate the bow shock profile practically instantaneously. Our model depends on the following solar wind parameters: polytropic index, sonic and Alfvén Mach numbers and angle between the velocity and the magnetic field. If the angle between the vectors of interplanetary magnetic field and undisturbed solar wind velocity is arbitrary, the model has 7 parameters: the distance to the nose point of the shock, the skewing angle of the bow shock in the plane including solar wind magnetic field and velocity vectors, two curvature radii and 2 bluntnesses in that same plane and in the perpendicular plane, and an additional parameter describing the transition to the asymptotic downstream slope of the bow shock. The number of parameters reduces to 6 in the case of the interplanetary magnetic field perpendicular to the solar wind velocity since in this

case the skewing angle vanishes. In the case of the interplanetary magnetic field parallel to the solar wind velocity the model has only 4 parameters due to its axial symmetry. If the interplanetary magnetic field vanishes, the model reduced to an earlier gas-dynamic shock model (Verigin et al., 2003a). The current model is developed for axially symmetric obstacles, but it can be extended to non-axially symmetric magnetospheric obstacles in a way similar to that of a gas dynamic model (Verigin et al., 2003a).

Acknowledgments

The research conducted at the University of Michigan was funded by NASA MMS GI grant 80NSSC18K13. The research did not use any new data.

References

- Bieber, J. W. & Stone E. C. (1979). Energetic electron bursts in the magnetopause electron layer and in interplanetary space. In *Magnetospheric Boundary Layers – A Sydney Chapman Conference*, (p. 131), ESA SP-148.
- Biermann, L., Brosowski, B., & Schmidt, H. U. (1967). The interaction of the solar wind with a comet. *Solar Physics*, 1, 254–284.
- Brecht, S.H. (1997). Hybrid simulation of the magnetic topology of Mars. *Journal of Geophysical Research: Space Physics*, 102, 4743-4750.
- Cairns, L. H. & Lyon, J. G. (1995). MHD simulations of the Earth's bow shock at low Mach numbers: Stand-off distances. *Journal of Geophysical Research: Space Physics*, 100(A9), 17173-17180.
- Chao, J. K., Wu, D. J., Lin, C.-H., Yang, Y.-H., Wang, X. Y., Kessel, M., Chen, S.H., & Lepping, R.P. (2002). Models for the size and shape of the Earth's magnetopause and bow shock. In: L.-H. Lyu (Ed.), *Space Weather Study Using Multipoint Techniques* (pp.360-368), Pergamon Press.
- Chapman, J. F. & Cairns, I. H. (2003). Three-dimensional modeling of Earth's bow shock: Shock shape as a function of Alfvén Mach number. *Journal of Geophysical Research: Space Physics*, 108(A5), 1174. <https://doi.org/10.1029/2002JA009569>.
- Chapman, J. F., Cairns, I. H., Lyon, J. G., & Boshuizen, C. R. (2004). MHD simulations of Earth's bow shock: Interplanetary magnetic field orientation effects on shape and position. *Journal of Geophysical Research: Space Physics*, 109, A04215. <https://doi.org/10.1029/2003JA010235>.
- Dmitriev, A. V., Chao, J. K., & Wu, D.-J. (2003). Comparative study of bow shock models using Wind and Geotail observations. *Journal of Geophysical Research: Space Physics*, 108(A12), 1464, <https://doi.org/10.1029/2003JA010027>.
- Fairfield, D. H. (1971). Average and unusual locations of the Earth's magnetopause and bow shock. *Journal of Geophysical Research: Space Physics*, 76(28), 6700-6716.
- Fairfield, D. H., Cairns I. H., Desch, M. D., Szabo, A., Lazarus, A. J., & Aellig, M. R. (2001). The location of low Mach number bow shocks at Earth, *Journal of Geophysical Research: Space Physics*, 106(A11), 25361-25376.

- Formisano, V. (1979). Orientation and shape of the Earth's bow shock in three dimensions, *Planetary and Space Science*, 27, 1151-1161.
- Gombosi, T. I. (1999). *Physics of the Space Environment*, Cambridge University Press, Cambridge.
- Hall, B. E. S., Sánchez- Cano, B., Wild, J. A., Lester, M., & Holmstrom, M. (2019). The Martian bow shock over solar cycle 23–24 as observed by the Mars Express mission. *Journal of Geophysical Research: Space Physics*, 124, 4761–4772, <https://doi.org/10.1029/2018JA026404>.
- Jelínek, K., Němeček, Z., & Šafránková, J. (2012). A new approach to magnetopause and bow shock modeling based on automated region identification. *Journal of Geophysical Research: Space Physics*, 117, A05208. <https://doi.org/10.1029/2011JA017252>.
- Kabin, K., Gombosi, T.I., DeZeeuw, D.L., & Powell, K.G. (2000). Interaction of Mercury with the solar wind. *Icarus*, 143, 397-406.
- Kabin, K. (2001) A note on the compression ratio in MHD shocks. (2001). *Journal of Plasma Physics*, 66(4), 259– 274.
- Kotova, G., Verigin, M., Zastenker, G., Nikolaeva, N., Smolkin, B., Slavin, J., et al. (2005). Bow shock observations by Prognoz–Prognoz 11 data: analysis and model comparison. *Advances in Space Research*, 36, 1958-1963.
- Kotova, G. A., Verigin, M. I., & Bezrukikh, V. V. (2015). Physics-based reconstruction of the 3-D density distribution in the entire quiet time plasmasphere from measurements along a single pass of an orbiter. *Journal of Geophysical Research: Space Physics*, 120, 7512–7521, <https://doi.org/10.1002/2015JA021281>.
- Kotova, G. A., Verigin, M. I., Gombosi, T., Kabin, K., & Bezrukikh, V. V. (2020a). Analytical description of the near planetary bow shock based on gas-dynamic and magneto-gas–dynamic modeling for the magnetic field parallel and perpendicular to the plasma flow. *Geomagnetism and Aeronomy*, 60(2), 164–172. <https://doi.org/10.1134/S0016793220020073>
- Kotova, G. A., Verigin, M. I., Gombosi, T., & Kabin, K. (2020b). Analytical model of the planetary bow shock for various magnetic field directions based on MHD calculations. *Solar-Terrestrial Physics*, 6(4), 98-104. <https://doi.org/10.12737/stp-64202007>.
- Ledvina, S.A., Ma, Y.-J., & Kallio, E. (2008). Modeling and simulating flowing plasmas and related phenomena, *Space Science Reviews*, 139, 143-189. <https://doi.org/10.1007/s11214-008-9384-6>, 2008.
- Lu, J. Y., Zhou, Y., Ma, X., Wang, M., Kabin, K., & Yuan, H. Z. (2019). Earth's bow shock: A new three-dimensional asymmetric model with dipole tilt effects, *Journal of Geophysical Research: Space Physics*, 124, 5396-5407. <https://doi.org/10.1029/2018JA026144>.
- Mejnertsen, L., Eastwood, J. P., Hietala, H., Schwartz, S. J., & Chittenden, J. P. (2018). Global MHD simulations of the Earth's bow shock shape and motion under variable solar wind conditions. *Journal of Geophysical Research: Space Physics*, 123, 259–271, <https://doi.org/10.1002/2017JA024690>.
- Merka, J., Szabo, A., Narock, T.W., King, J.H., Paularena, K.I., & Richardson, J.D. (2003). A comparison of IMP 8 observed bow shock positions with model predictions. *Journal of Geophysical Research: Space Physics*, 108(A2), 1077. <https://doi.org/10.1029/2002JA009384>.

- Meziane, K., Alrefay, T.Y., & Hamza, A. (2014) On the shape and motion of the Earth's bow shock, *Planetary and Space Science*, 93-94, 1–9, <https://doi.org/10.1016/j.pss.2014.01.006>.
- Němeček, Z. & Šafránková, J. (1991). The Earth's bow shock and magnetopause position as a result of solar wind-magnetosphere interaction. *Journal of Atmospheric and Terrestrial Physics*, 53, 1049-1054.
- Peredo, M., Slavin, J.A., Mazur, E., & Curtis, S.A. (1995). Three-dimensional position and shape of the bow shock and their variation with Alfvénic, sonic and magnetosonic Mach numbers and interplanetary magnetic field orientation, *Journal of Geophysical Research: Space Physics*, 100(A5), 7907-7916.
- Petrinec S.M., & Russell C.T. (1997). Hydrodynamic and MHD equations across the bow shock and along the surfaces of planetary obstacles, *Space Science Reviews*, 79, 757-791.
- Pokhotelov, D., von Alfthan, S., Kempf, Y., Vainio, R., Koskinen, H. E. J., & Palmroth, M. (2013). Ion distributions upstream and downstream of the Earth's bow shock: first results from Vlasiator, *Annales Geophysicae*, 31, 2207–2212. <https://doi.org/10.5194/angeo-31-2207-2013>.
- Slavin, J.A. & Holzer, R.E. (1981). Solar wind flow about the terrestrial planets, 1, Modeling bow shock position and shape, *Journal of Geophysical Research: Space Physics*, 86(A13), 11401-11418.
- Slavin, J.A., Holzer, R. E., Spreiter, J. R., & Stahara, S. S. (1984). Planetary Mach cones: Theory and observation. *Journal of Geophysical Research: Space Physics*, 89, 2708.
- Stahara, S. (2002). Adventures in the magnetosheath: two decades of modeling and planetary applications of the Spreiter magnetosheath model. *Planetary and Space Science*, 50, 421-442. [https://doi.org/10.1016/S0032-0633\(02\)00023-5](https://doi.org/10.1016/S0032-0633(02)00023-5).
- Verigin, M.I. (2004). Position and shape of near planetary bow shocks: Gasdynamic and MHD aspects. In B.M. Shevtsov (Ed.) *Solar-terrestrial connections and electromagnetic precursors of earthquakes: Proceedings of III Intern. conf.*, (pp. 49-69), Kamchatka region, 16–21 August 2004 /. – Petropavlovsk-Kamchatsky: IKIR FEB RAS, (in Russian).
- Verigin, M.I., Kotova, G.A, Remizov, A.P., Shutte, N.M., Schwingenschuh, K., Riedler, W., et al. (1997a). Studies of the Martian bow shock response to the variation of the magnetosphere dimensions according to TAUS and MAGMA measurements aboard the PHOBOS 2 orbiter. *Advances in Space Research*, 20(2), 155-158.
- Verigin, M., Kotova, G., Shutte, N., Remizov, A., Szegő, K., Tátrallyay, M., et al. (1997b). Quantitative model of the Martian magnetopause shape and its variation with the solar wind ram pressure based on Phobos 2 observations, *Journal of Geophysical Research: Space Physics*, 102(A2), 2147-2155.
- Verigin, M. I., Kotova, G. A., Remizov, A. P., Styashkin, V. A., Shutte, N. M., Zhang, T.-L., et al. (1999). Shape and location of planetary bow shocks, *Cosmic Research*, 37(1), 34-39.
- Verigin, M., Kotova, G., Szabo, A., Slavin, J., Gombosi, T., Kabin, et al (2001a). WIND observations of the terrestrial bow shock 3-d shape and motion, *Earth, Planets and Space*, 53(10), 1001-1009.

- Verigin, M.I., Kotova, G.A., Slavin, J., Szabo, A., Kessel, M., Safrankova, J., et al. (2001b). Analysis of the 3-D shape of the terrestrial bow shock by Interball/Magion 4 observations, *Advances in Space Research*, 28(6), 857-862.
- Verigin, M., Slavin, J., Szabo, A., Gombosi, T., Kotova G., Plochova O., et al. (2003a). Planetary bow shocks: Gasdynamic analytic approach, *Journal of Geophysical Research: Space Physics*, 108(A8), 1323, <https://doi.org/10.1029/2002JA009711>.
- Verigin, M., Slavin, J., Szabo, A., Kotova, G., & Gombosi, T. (2003b). Planetary bow shocks: Asymptotic MHD Mach cones. *Earth, Planets and Space*, 55, 33-38.
- Verigin, M.I., Slavin, J., Szabo, A., Kotova, G.A., Remizov, A.P., Rosenbauer, H., et al. (2004a). Unusually Distant Bow Shock Encounters at Mars: Analysis of March 24, 1989 event, *Space Science Reviews*, 111: 233–243.
- Verigin, M., Vignes, D., Crider, D., Slavin, J., Acuña, M., Kotova, G., & Remizov, A. (2004b). Martian obstacle and bow shock: origins of boundaries anisotropy. *Advances in Space Research*, 33(12), 2222-2227.
- Verigin, M. I., Kotova, G. A., Bezrukikh, V. V., Zastenker, G. N., & Nikolaeva, N. (2009). Analytical model of the near Earth magnetopause according to the data of the Prognoz and Interball Satellites, *Geomagnetism and Aeronomy*, 49(8), 1176-1181. <https://doi.org/10.1134/S0016793209080283>.
- Verigin, M. I., Kotova, G. A., & Bezrukikh, V. V. (2018). Geomagnetopause position and shape dependence on solar wind plasma and IMF parameters: Analytic model comparison with observations and 3-D MHD runs. In C. Foullon & O.E. Malandraki (Eds.), *Proceedings IAU Symposium No. 335*, 2017, (pp. 121-124). <https://doi.org/10.1017/S1743921317010420>.
- Wallis, M. K. (1973). Weakly-shocked flows of the solar wind plasma through atmospheres of comets and planets. *Planetary and Space Science*, 21, 1647 – 1660.
- Wang, M., Lu, J. Y., Kabin, K., Yuan, H. Z., Zhou, Y., & Guan, H. Y. (2020). Influence of the interplanetary magnetic field cone angle on the geometry of bow shocks, *Astronomical Journal*, 159(5), 227. <https://doi.org/10.3847/1538-3881/ab86a7>.
- Winterhalter, D., Kivelson, M.G., Walker, R.J., & Russell, C.T. (1984). The MHD Rankine-Hugoniot jump conditions and the terrestrial bow shock: A statistical comparison. *Advances in Space Research*, 4(2-3), 287-292. [https://doi.org/10.1016/0273-1177\(84\)90323-5](https://doi.org/10.1016/0273-1177(84)90323-5).

Figure captions

Figure 1. Bow shock parameters used in our model: r_o , r_s are positions of the obstacle boundary and bow shock nose, respectively; R_o , R_s are nose curvature radii; respectively; and Δ is the bow shock standoff distance; ω is the slope of the bow shock.

Figure 2. Definitions of the additional bow shock parameters for arbitrary direction of the interplanetary magnetic field..

Figure 3. Calculations of α_{vn} for different Mach numbers and angles \mathcal{G}_{bv} . Asterisks mark fitting of skewing angles (see section 6).

Figure 4. $t^2(p)$ function for $M_S = 6$, $M_A = 3$, $\mathcal{G}_{bv} = 70^\circ$, $\alpha_{vn} = 4.3^\circ$. Sections of $t^2(p)$ shown with solid blue lines are physically meaningful; those shown with blue dashed lines do not correspond to real shocks. The vertical dashed lines represent the asymptotes of this function.

Figure 5. Example of the grid. Cut cells used to fit the central body are not shown.

Figure 6. Parameters $r_s(\varphi_s)$, $R_s(\varphi_s)$ and $b_s(\varphi_s)$ as functions of the angle φ_s . Points are the parameters of approximation of MHD simulations in planes $\varphi_s = \text{const}$ with a step along φ_s equal to 5° , solid lines - approximation using expressions (21).

Figure 7. Two examples of fitting the MHD bow shock calculations (black points) with relation (1): a,c – blue line shows fitting in the (X,Y) plane of the GIPM system, red line shows fitting in the (X,Z) plane; b, d – cross-sections of the bow shock by planes $X = \text{const}$, hot pink points.

Figure 8. Comparison of the parameters r_s , R_{sy} and R_{sz} of the bow shock model (1) fitting the MHD calculations (Table 1), with the parameters calculated using the GD model. Dashed lines represent fitting dependencies, printed at the bottom of each panel.

Figure 9. a - Interrelationship between the parameters b_{sy} and b_{sz} , b – comparison for the parameter b_{sz} fitting the MHD calculations, with the parameter b_{sz_norm} , calculated using the GD model, c – comparison of the fitting parameter d_s with calculated parameter d_{s_norm} . Dashed black lines show fitting dependencies printed at the bottom of the panels.

Figure 10. Two examples comparing the MHD bow shock calculations (black points) with its location determined by relations (1, 6, 27-30): a, c – blue line shows expression (1) in the (X,Y) plane of GIPM system, red line shows expression (1) in the (X,Z) plane; b, d – cross-sections of the bow shock by planes $X = \text{const}$, hot pink points - expression (1).

Table 1

No	γ	b_o	M_S	M_A	\mathcal{G}_{bv}	Shock parameters obtained by fitting the MHD simulations								σ 10^{-4}
						r_s	R_{SY}	R_{SZ}	b_{SY}	b_{SZ}	d_s	α_{vn}	α_{vz}	
1	5/3	-1	6	3	20°	1.252	1.743	1.814	-0.234	0.41	2.65	7.3°	5.92°	8.55
2	5/3	-1	6	5	20°	1.234	1.623	1.645	-0.348	-0.224	1.15	3.6°	2.03°	1.93
3	5/3	0	6	5	30°	1.304	1.956	2.097	0.424	0.544	0.37	3.5°	2.68°	2.24
4	2.0	-1	6	5	30°	1.327	1.789	1.816	-0.328	-0.142	1.05	4.0°	1.86°	1.57
5	5/3	-1	8	5	30°	1.252	1.62	1.628	-0.544	-0.216	1.225	4.6°	2.80°	3.19
6	5/3	0	6	5	60°	1.406	2.137	2.393	0.286	0.53	0.24	2.8°	2.48°	2.31
7	2.0	0	6	5	60°	1.504	2.383	2.636	0.414	0.686	0.475	2.6°	1.78°	1.58
8	5/3	-1	8	5	60°	1.322	1.685	1.75	-0.572	-0.132	0.955	4.0°	2.60°	2.77
9	5/3	-1	6	3	70°	1.489	1.933	2.192	-0.308	0.378	0.9	5.4°	4.33°	12.5
10	2.0	-1	6	5	70°	1.394	1.875	1.952	-0.444	-0.092	1.065	3.5°	1.31°	1.4
11	5/3	-1	6	5	70°	1.342	1.834	1.85	-0.92	-0.164	1.6	2.9°	1.80°	2.08
12	5/3	-1	6	2	45°	1.516	2.662	3.005	-0.982	0.366	3.075	12.9°	15.68°	10.9
13	5/3	-1	6	3	45°	1.374	1.91	2.072	-0.646	0.322	1.6	9.5°	7.86°	27.7
14	5/3	-1	6	5	45°	1.294	1.725	1.773	-0.568	-0.178	1.18	4.7°	2.98°	2.88
15	2.0	0	6	5	0°	1.327	2.11	2.11	0.5	0.5	0.3	0°	0°	0.22
16	2.0	-1	6	5	0°	1.284	1.685	1.685	-0.373	-0.373	2.56	0°	0°	0.18
17	5/3	0	6	3	0°	1.201	1.96	1.96	0.93	0.93	0.5	0°	0°	0.2
18	5/3	0	6	5	0°	1.238	1.88	1.88	0.404	0.404	0.16	0°	0°	0.68
19	5/3	-1	6	3	0°	1.181	1.67	1.67	0.2	0.2	0.4	0°	0°	0.4
20	5/3	-1	6	5	0°	1.214	1.49	1.49	-0.15	-0.15	1.5	0°	0°	0.4
21	5/3	-1	8	5	0°	1.201	1.46	1.46	-0.03	-0.03	0.3	0°	0°	0.28
22	2.0	-1	6	5	90°	1.431	1.858	1.934	-0.245	0.095	0.54	0°	0°	0.68
23	5/3	0	6	5	90°	1.452	2.22	2.51	0.23	0.51	0.16	0°	0°	0.32
24	5/3	-1	6	3	90°	1.524	1.918	2.18	-0.145	0.35	0.52	0°	0°	0.47
25	5/3	-1	6	5	90°	1.361	1.722	1.806	-0.445	-0.005	0.86	0°	0°	0.21
26	5/3	-1	8	5	90°	1.358	1.612	1.768	-0.18	0.01	0.22	0°	0°	0.25

Appendix

Formulas for calculating the parameters of the bow shock model in the gas-dynamic approximation are collected here for the convenience of using our analytical model (Appendix 1 in Kotova et al, 2020b; Eq. 35-38 in Verigin et al., 2003a, (note, that equation (36) of Verigin 2003 had a misprint, corrected by Kotova et al, 2020b.)

In the gas-dynamic approximation

$$\varepsilon = \frac{(\gamma-1)M_S^2+2}{(\gamma+1)M_S^2} \quad (1a)$$

$$\varepsilon^* = \frac{\varepsilon}{1-\varepsilon} \quad (2a)$$

$$\xi = \varepsilon^* + \frac{\gamma+1}{50} \left(\varepsilon^* - \frac{\gamma-1}{2} \right) \quad (3a)$$

$$r_s = r_o + \frac{1.229c(b_o)R_o\xi^{2/3}}{\left(1+\frac{\gamma+1}{50}\right)^{2/3}(\gamma+1)^{1/3}} \left(1 - \frac{b(b_o,\gamma)}{\xi^{1/6}}\right) \quad (4a)$$

$$R_s = 3c(b_o)R_o\xi^{5/3} \left(\frac{1}{(1+\gamma)^{4/3}\left(1+\frac{\gamma+1}{50}\right)^{5/3}} + \frac{a(b_o,\gamma)}{\xi d(b_o)} \right) \quad (5a)$$

$$b_s = \frac{1}{M_S^2-1} + e(b_o,\gamma) + \frac{M_S^2+1}{M_S^4} \cdot \frac{\frac{21}{17}(e(b_o,\gamma))^2 - \frac{14}{9}e(b_o,\gamma) + \frac{7}{4}}{1 - \frac{23}{30}e(b_o,\gamma)} \quad (6a)$$

$$d_s = \exp\left(\frac{107}{29} - \frac{371}{68} \left(\frac{8}{13}\left(b_o - \frac{4}{21}\right) + \left(1 + \left|\frac{8}{13}\left(b_o - \frac{4}{21}\right)\right|^{11/7}\right)^{7/11}\right)\right) \quad (7a)$$

where

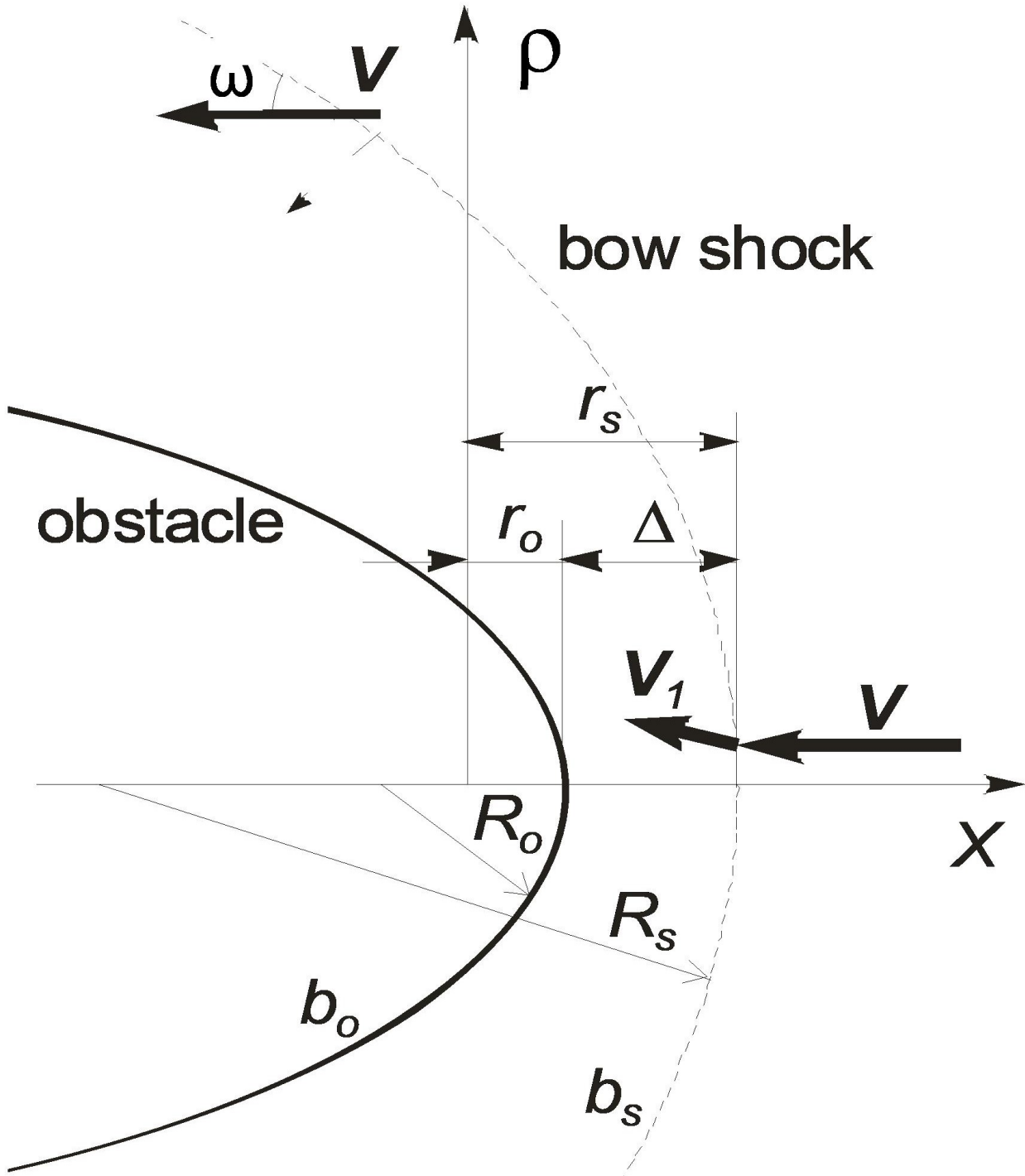
$$a(b_o,\gamma) = \frac{1}{2} \left(\frac{52}{25} + \frac{97}{84} - \frac{33}{10} \left(\frac{1}{(\gamma+1)^{13/4}} - \left(\frac{5}{12}\right)^{13/4} \right) \right) \cdot \left(1 - \frac{\frac{7}{16}b_o}{\left(1 + \left|\frac{7}{16}b_o\right|^{8/33}\right)^{33/8}} \right) - \frac{97}{84} + \frac{33}{10} \left(\frac{1}{(\gamma+1)^{13/4}} - \left(\frac{5}{12}\right)^{13/4} \right) \quad (8a)$$

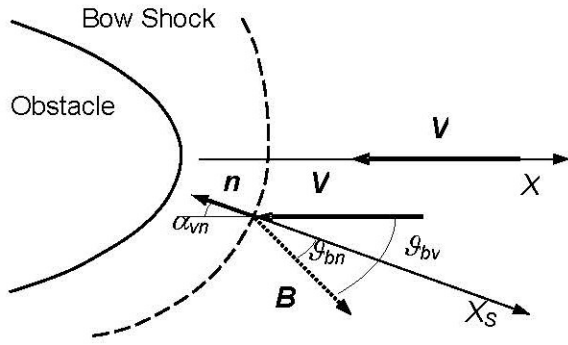
$$b(b_o,\gamma) = \frac{1}{2} \left(-\frac{23}{35} + \frac{43}{3} \left(\frac{1}{(\gamma+1)^{13}} - \left(\frac{5}{12}\right)^{68/13} \right) - \frac{24}{13} + \frac{13}{18} \left(\frac{1}{\gamma^{13}} - \left(\frac{5}{7}\right)^{57/13} \right) \right) \cdot \left(1 - \frac{b_o - \frac{3}{10}}{\left(\left(\frac{119}{20}\right)^2 + \left|b_o - \frac{3}{10}\right|^2\right)^{1/2}} \right) + \frac{24}{13} - \frac{13}{18} \left(\frac{1}{\gamma^{13}} - \left(\frac{5}{7}\right)^{57/13} \right) \quad (9a)$$

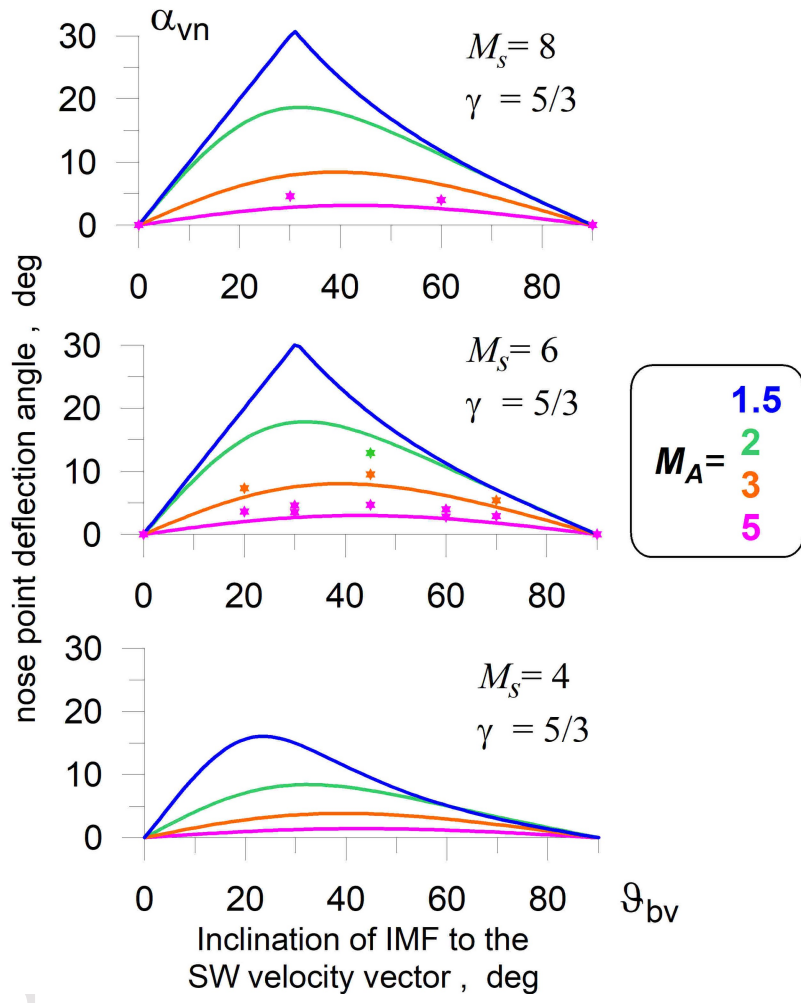
$$c(b_o) = \frac{6}{5} \left(\frac{17}{20} b_o + \left(1 + \left| \frac{17}{20} b_o \right|^{\frac{5}{3}} \right)^{\frac{3}{5}} \right) + \frac{\frac{41}{52}}{\left(\left(\frac{26}{9} \right)^2 + b_o^2 \right)^{\frac{1}{4}}} \quad (10a)$$

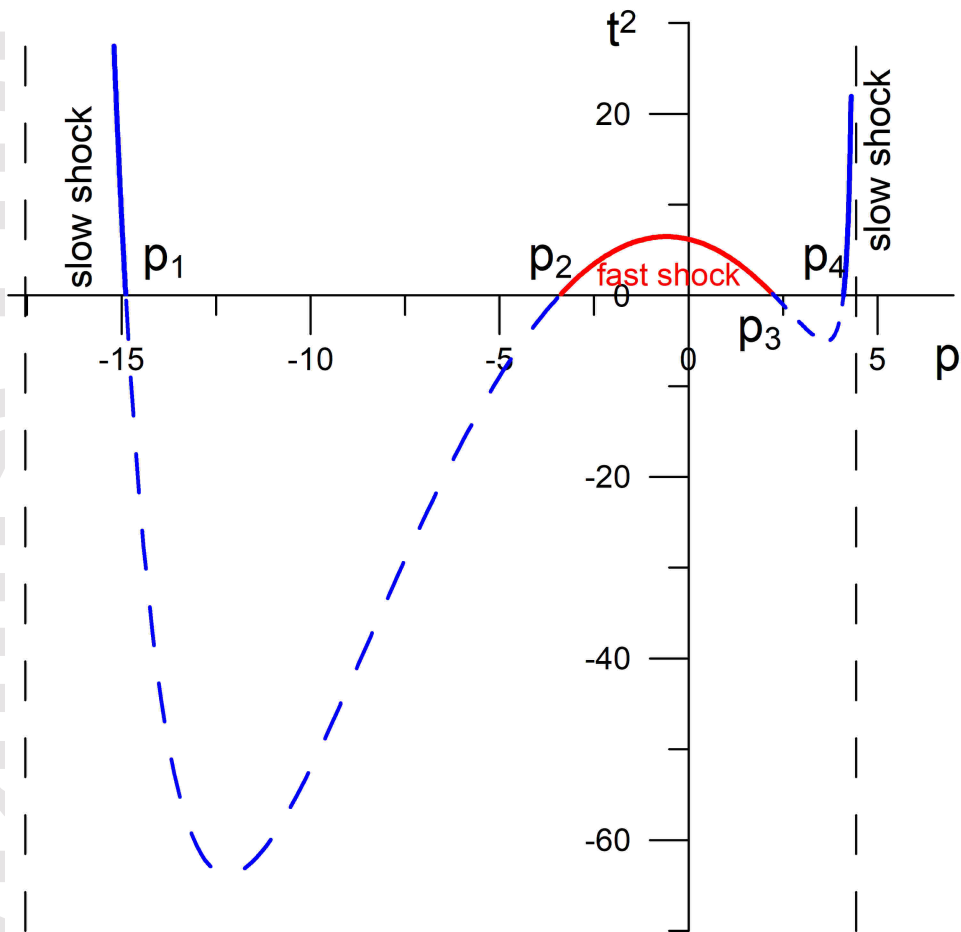
$$d(b_o) = \frac{1}{2} \left(\frac{85}{47} - \frac{15}{29} \right) \left(1 - \frac{19}{33} \frac{\left(b_o - \frac{39}{70} \right)}{\left(1 + \left| \frac{19}{33} \left(b_o - \frac{39}{70} \right) \right|^{\frac{5}{6}} \right)^{\frac{6}{5}}} \right) + \frac{15}{29} \quad (11a)$$

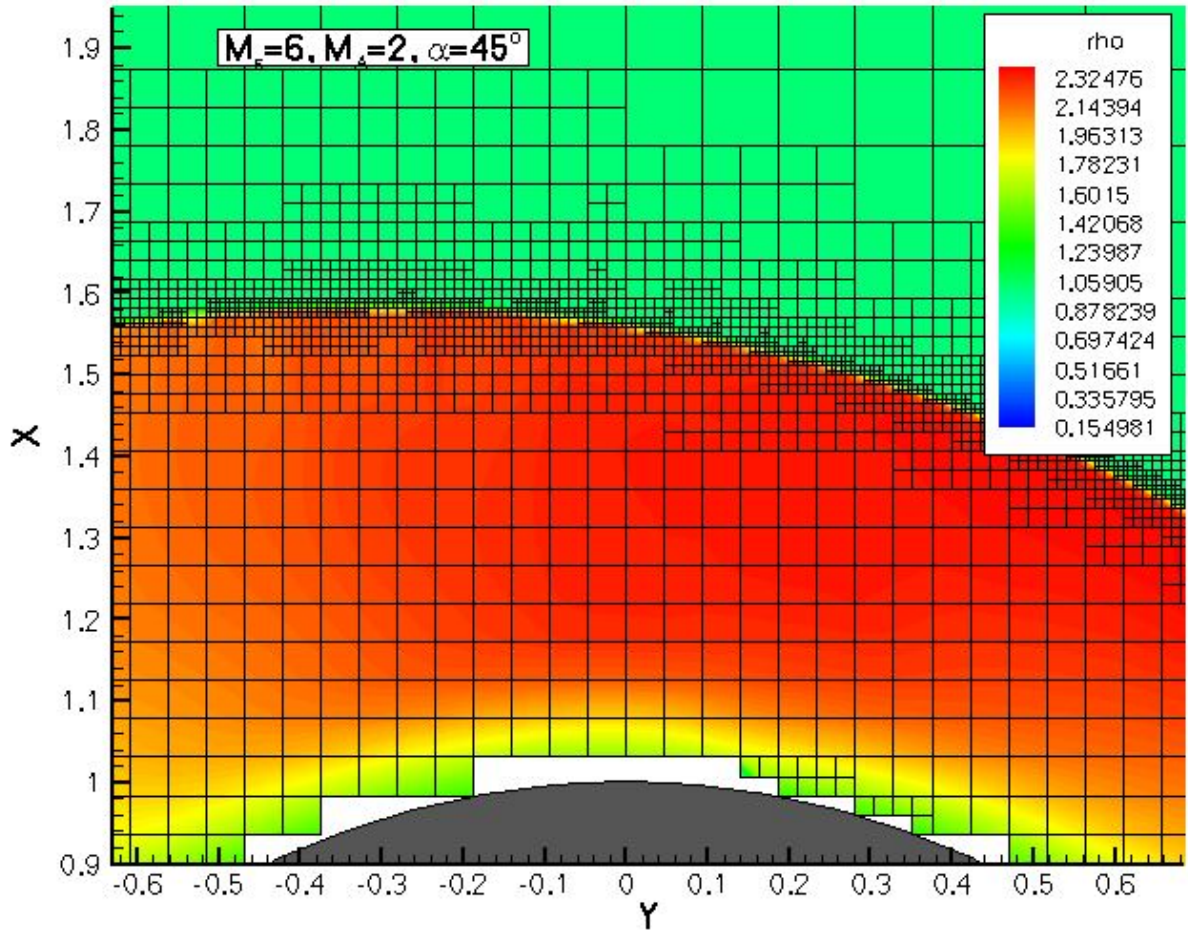
$$e(b_o, \gamma) = \frac{1}{2} \left(-\frac{1042}{17} - 40 \left(\frac{1}{\gamma^{\frac{15}{4}}} - \left(\frac{5}{7} \right)^{\frac{15}{4}} \right) - \frac{1318}{39} \right) \cdot \left(1 - \frac{\left(b_o + \frac{841}{61} + \frac{160}{11} \left(\frac{1}{\gamma^{\frac{16}{5}}} - \left(\frac{5}{7} \right)^{\frac{16}{5}} \right) \right)}{\left(\left(\frac{809}{18} \right)^2 + \left(b_o + \frac{841}{61} + \frac{160}{11} \left(\frac{1}{\gamma^{\frac{16}{5}}} - \left(\frac{5}{7} \right)^{\frac{16}{5}} \right) \right)^2 \right)^{\frac{1}{2}}} \right) + \frac{1318}{39} \quad (12a)$$











$\gamma = 5/3, b_o = 0, M_S = 6, M_A = 5, \vartheta_{bv} = 60^\circ, \alpha_{vn} = 2.5^\circ$

